# Supporting Information

# Theoretical guidance for targeted modulation of metal-nitrogen single atom active sites on 3D porous carbon to optimize electrocatalytic performance in energy conversion applications

Tianxiang Yang [a, 1], Yongwei Zhang [a, 1], Jing Shi [b], Guangping Yang [a], Jiaoe Dang [a], Meonglong Sun [a], Asim Arshad [a], Nosheen Zafar [c], Sining Yun [a *]

[a.] Functional Materials Laboratory (FML), School of Materials Science and Engineering, Xi'an University of Architecture and Technology, Xi'an, Shaanxi, 710055, China. Fax: (+86)29-82205245; Tel: (+86)29-82205245

[b.] Department of Physics, Xi'an Jiaotong University, Xi'an, Shaanxi 710018, China

[c.] Department of Physics, University of Engineering and Technology, Lahore 54890, Pakistan

[1] These authors contributed equally

**Corresponding author:** Prof. Sining Yun

E-mail: alexsyun1974@aliyun.com; yunsining@xauat.edu.cn

## Materials characterizations

The morphological characteristics and structural properties of Ni-NDPC, Cu/Ni-NDPC, Mo/Ni-NDPC, and Fe/Ni-NDPC were measured via field emission scanning electron microscope (FESEM, Germany, MERLIN Compact, ZEISS), transmission electron microscopy (TEM, America, ThermoFisher Talos F200X), and conjoined with the X-ray diffractometer (XRD, America, D/Max 2200, MDI). The surface information and defect/graphitic information of Ni-NDPC and M/Ni-NDPC were measured via X-ray photoelectron spectroscopy (XPS, America, Thermo ESCALAB 250XI) and Raman spectroscopy (France, LabRAM HR Evolution), respectively. The surface area and pore properties were measured via nitrogen adsorption-desorption measurement (ASAP2020, America). Atomic-level resolution images were obtained on a high-angle annular dark-field scanning/transmission electron microscope (HAADF-STEM, JEM-ARM200F, 200 kV) with an aberration-corrected probe. The X-ray absorption fine structure (XAFS) spectra were performed collected at 1W1B station in Beijing Synchrotron Radiation Facility (BSRF). The raw EXAFS data were background-subtracted, normalized and Fourier transformed by the standard procedures using the Athena module and Hephaestus module implemented in the IFEFFIT software packages. The coordination parameters were obtained by a least square fit in the R-space, k-weighted Fourier transformed data using Artemis.

**Electrochemical characterization for IRR**

The Electrochemical characterization including cyclic voltammetry (CV), EIS, and Tafel polarization tests was evaluated by using an electrochemical workstation (CHI 660E, Chenhua, Shanghai, China). Cyclic voltammetry (CV) measurement of catalysts was conducted in a three-electrodes system which is composed of $Ag/Ag^{+}$ (reference electrode), Pt (counter electrode), and as-prepared IRR electrode (working electrode), and acetonitrile electrolyte (containing 10 mM LiI, 0.1 M $LiClO_4$, and 1 mM $I_2$). The EIS results were fitted via Z-view software. The *J-V* curves of the liquid-junction solar cells were measured using a solar simulator (USA, EASISOLAR-50-3A, CROWNTECH, INC.,) and a digital source meter (USA, Keithley 2400) under standard sunlight (AM 1.5, 100 mW $cm^{-2}$).

**Electrochemical characterization for HER**

The HER activity of electrocatalysts was evaluated by using a three-electrode system in 1 M KOH solution with the help of a CHI 660E electrochemical analyzer. This three-electrode system consists of graphite rod (counter electrode), HER electrode (working electrode), and Hg/HgO electrode (reference electrode). Linear sweep voltammetry (LSV) was measured with the 95% ohmic potential drop (iR) correction with the potential from -1.4 to -0.8 V with the scan rates of 5 mV $s^{-1}$. According to the Tafel equation, we deduced the Tafel slope curves from the LSV curves. EIS test was performed with an amplitude of 5 mV matched with the frequency from $10^5$ to $10^{-1}$ Hz. The long-term stability of electrocatalysts was performed by comparing the variation of LSV curves before and after 1000 cycles of the CV test. Chronopotentiometric measurements (CP) were conducted for 10 h. To avoid the influence of air in the system on the test results, the test system should be cleaned via the $N_2$. The potentials and reversible hydrogen electrode (RHE) were converted through the equation of $E$ (*vs.* RHE) = $E$ (*vs.* Hg/HgO) + 0.059 pH + 0.098.

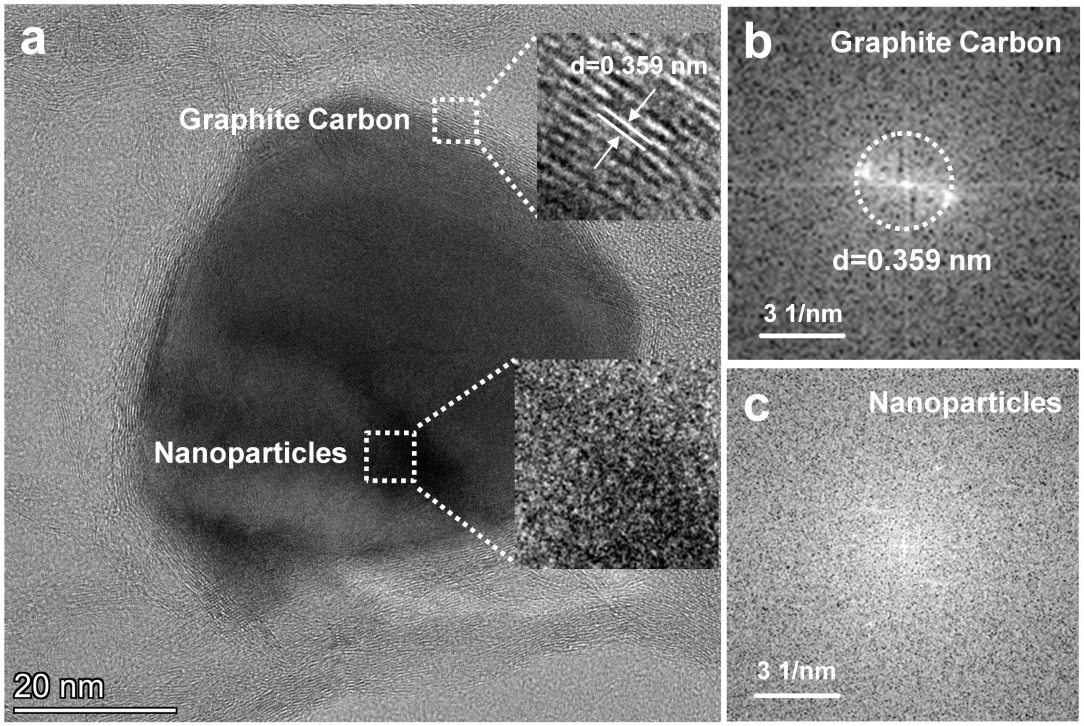


**Figure S1.** (a) HRTEM images of Fe/Ni-NDPC, FFT images of (b) nanoparticles regions and (c) graphitic carbon regions of Fe/Ni-NDPC.

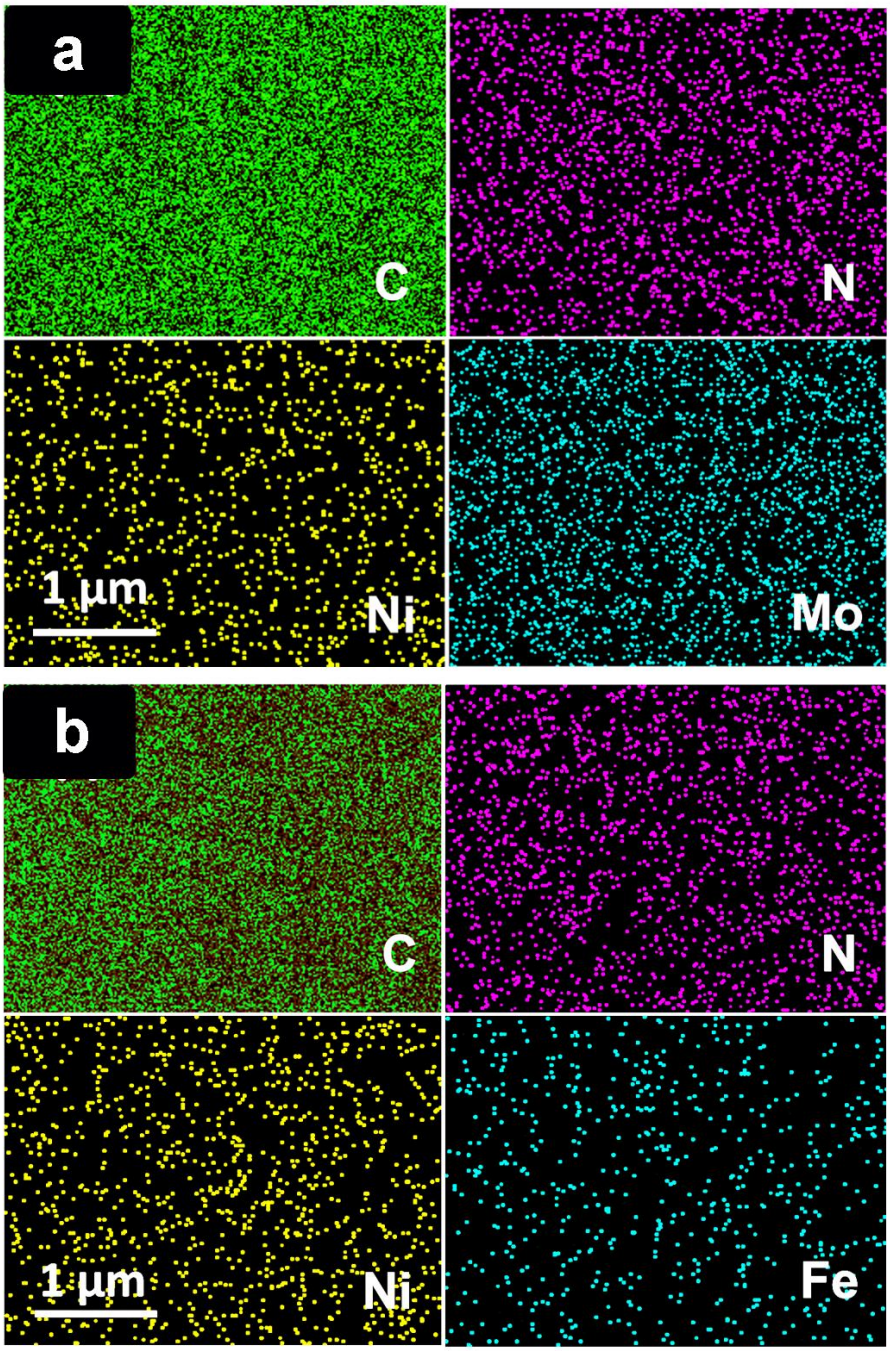


**Figure S2.** The EDS elemental mapping images of (a) Mo/Ni-NDPC and (b) Fe/Ni-NDPC.

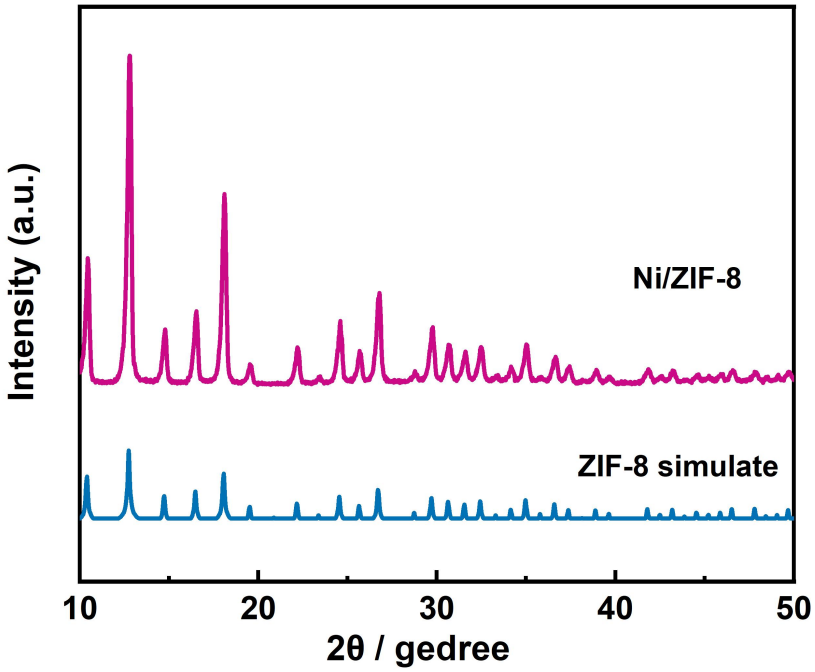


**Figure S3.** The XRD patterns of as-prepared (a) Ni/ZIF-8 and ZIF-8 simulate.

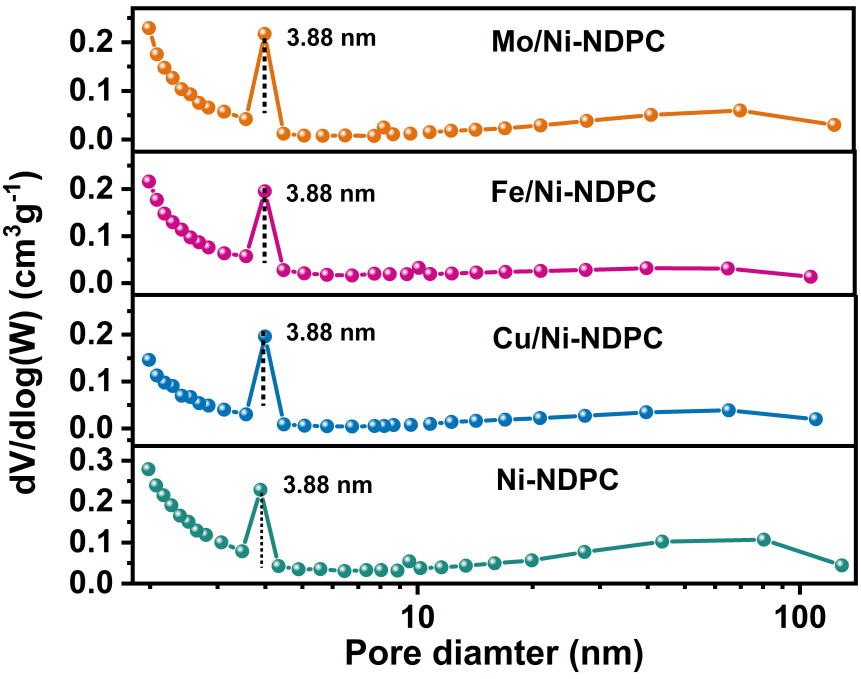


**Figure S4.** The pore size distribution of as-prepared catalysts.

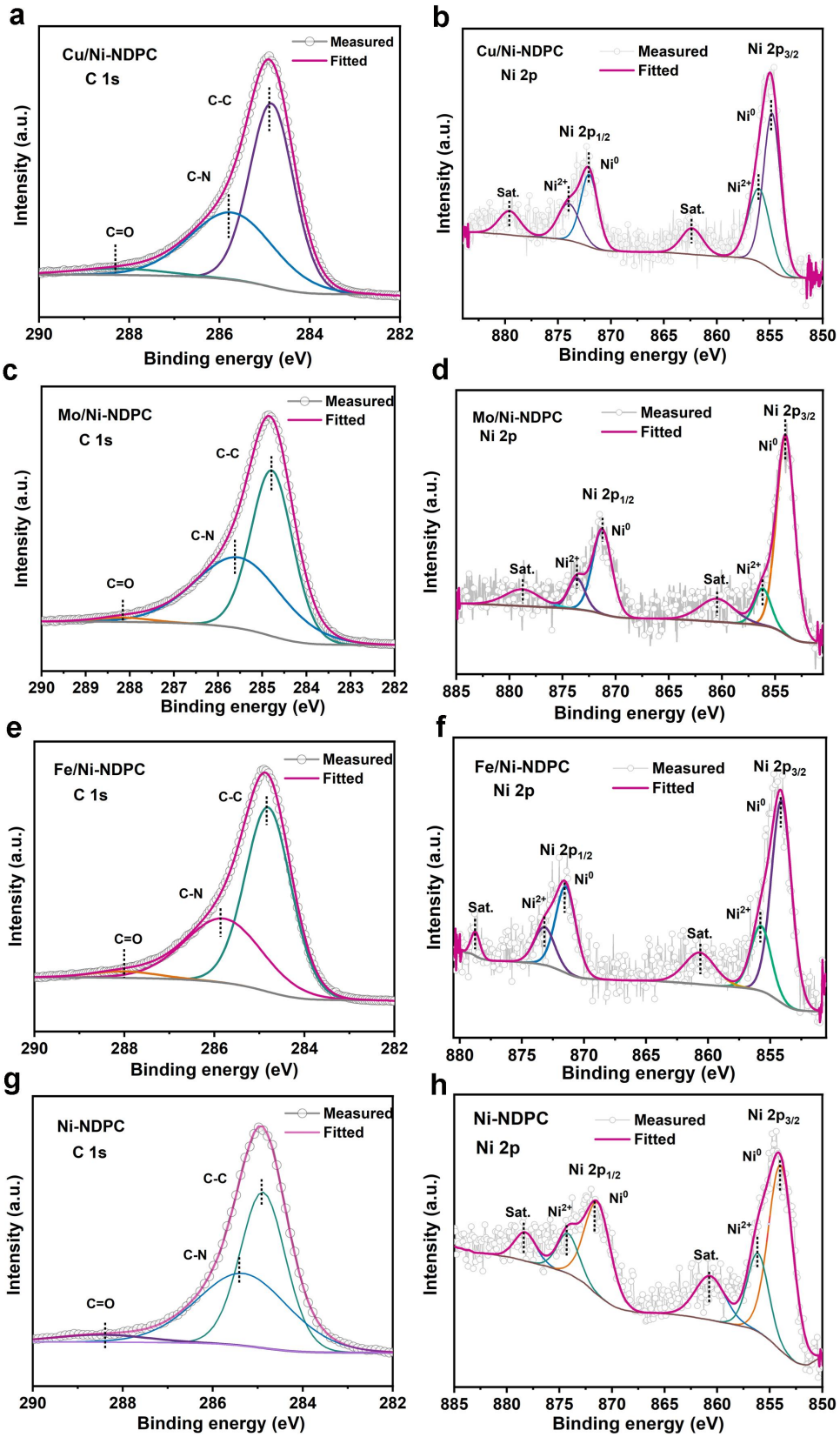


**Figure S5.** The high-resolution of Ni 2p and C 1s XPS spectrum in the (a)-(b) Cu/Ni-NDPC, (c)-(d) Mo/Ni-NDPC, (e)-(f) Fe/Ni-NDPC, and (g)-(h) Ni-NDPC catalysts, respectively.

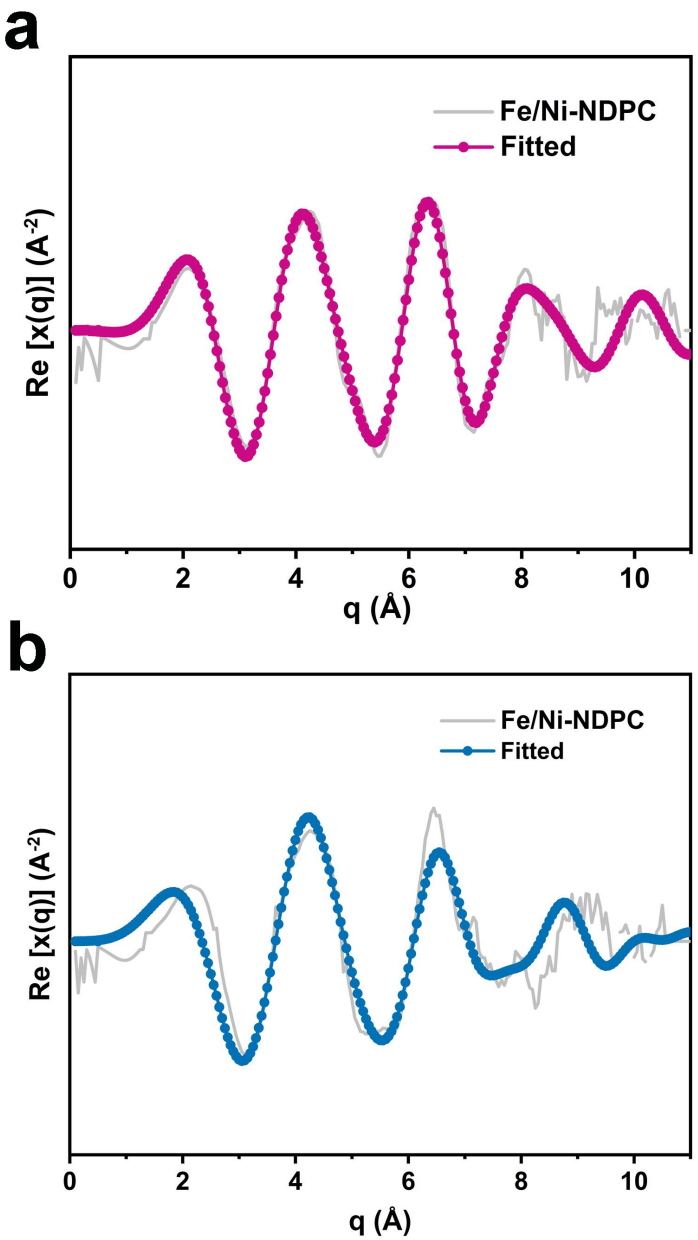


**Figure S6.** The corresponding (a) Fe K-edge and (b) Mo K-edge EXAFS fitting curves of Fe/Ni-NDPC at q space.

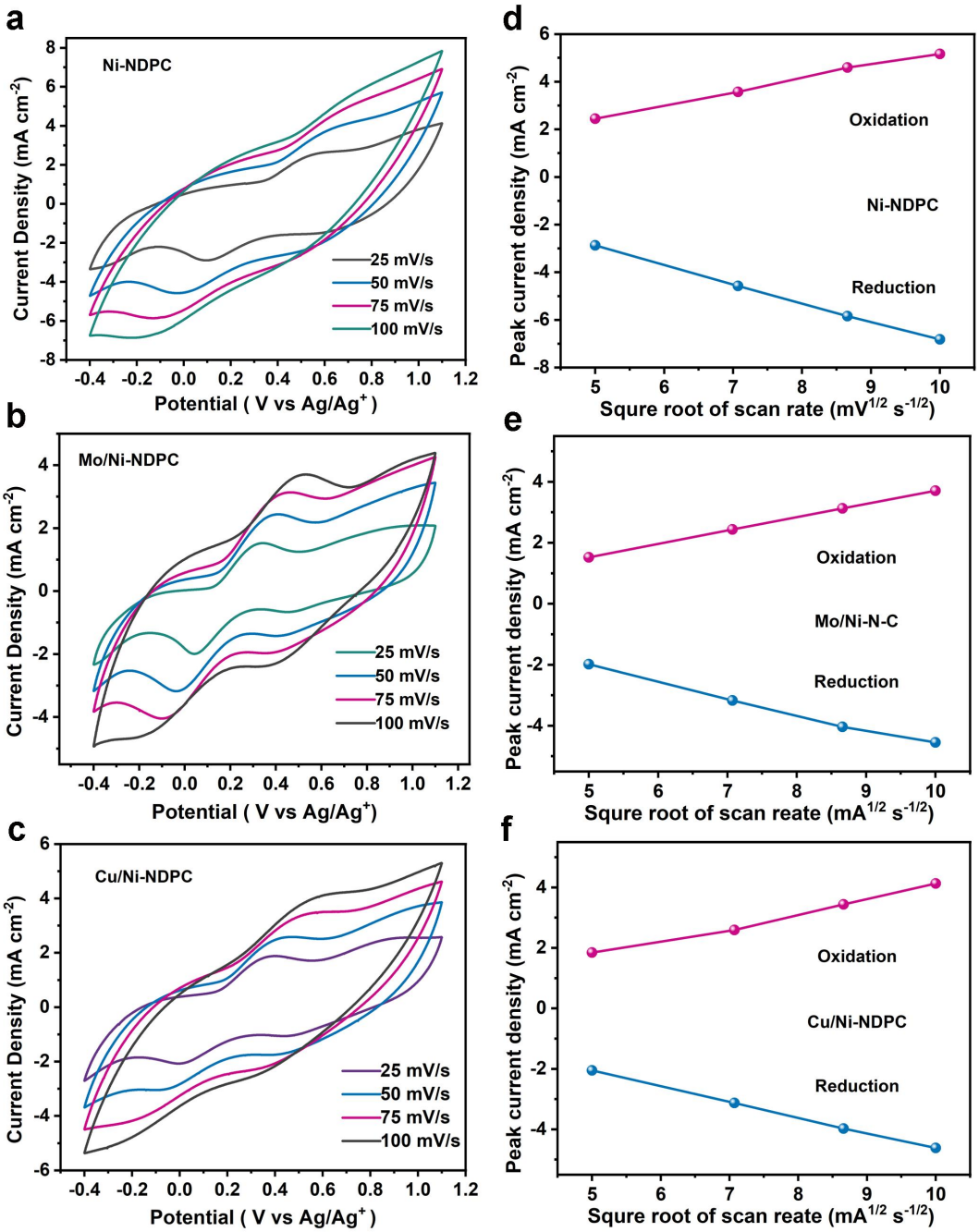


**Figure S7.** CV curves of (a) Ni-NDPC, (b) Mo/Ni-NDPC, and (c) Cu/Ni-NDPC at scan rates of 25, 50, 75, and 100 mV/s in $I^-/I_3^-$ electrolyte, respectively; the relation between peak current density and the square root of scan rate of CVs for (d) Ni-NDPC, (e) Fe/Ni-NDPC, and (f) Mo/Ni-NDPC CE.

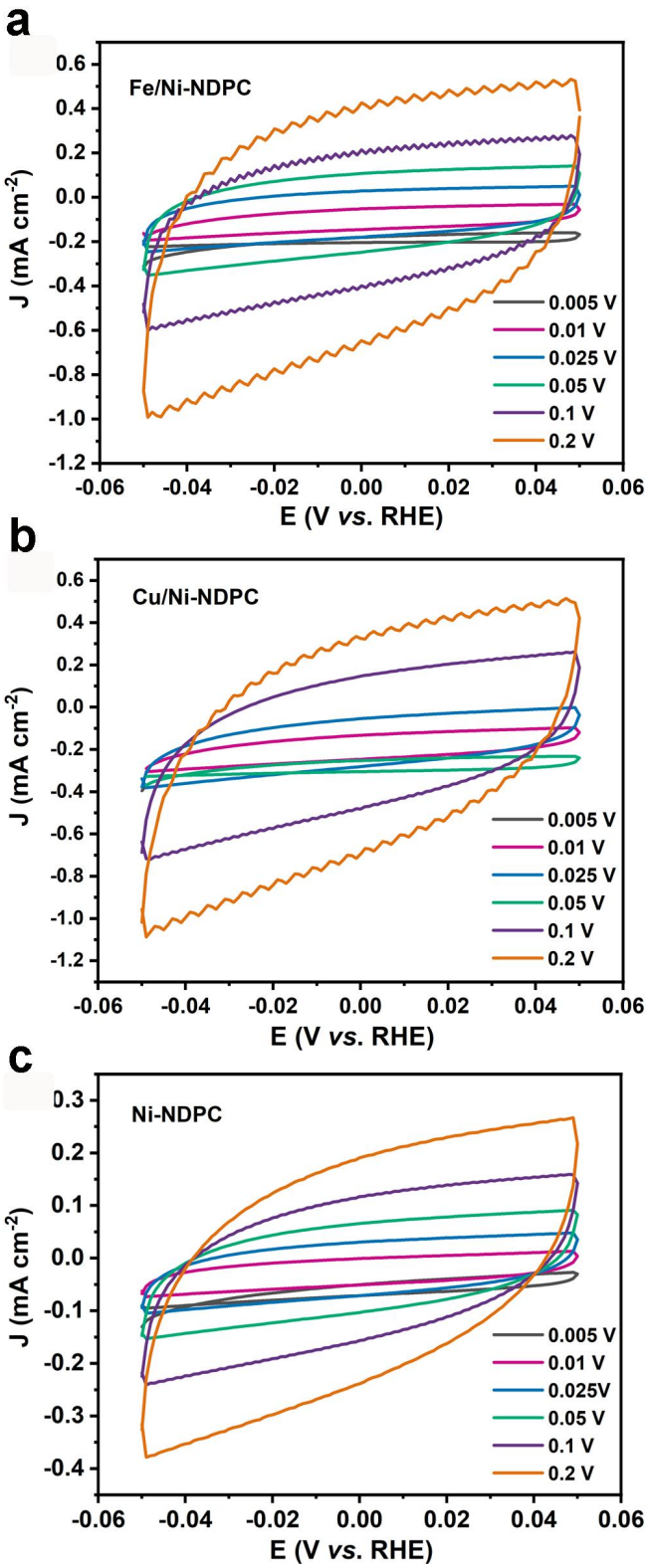


**Figure S8.** CV curves in a non-Faraday region (-0.06 – 0.06 V vs. Hg/HgO.

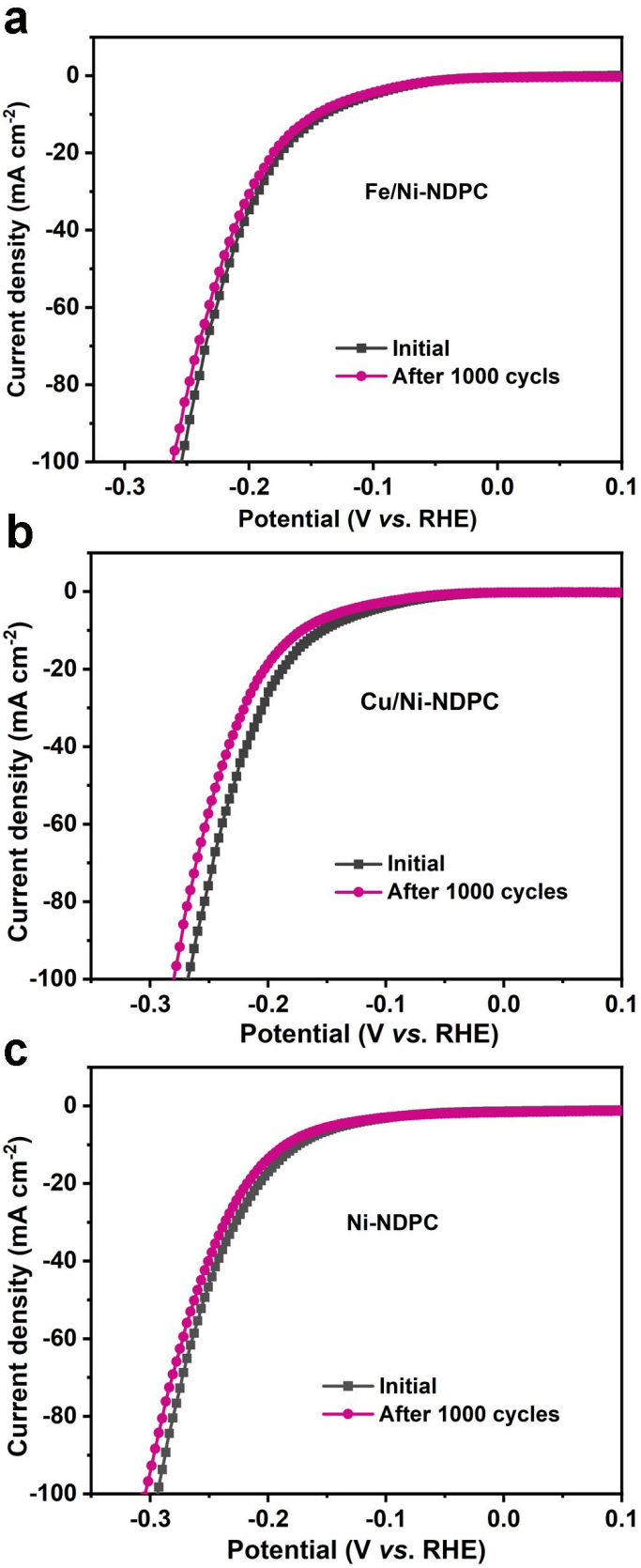


**Figure S9.** LSV curves of (a) Fe/Ni-NDPC, (b) Cu/Ni-NDPC, and (c) Ni-NDPC before and after 1000 CV cycles in 1 M KOH.

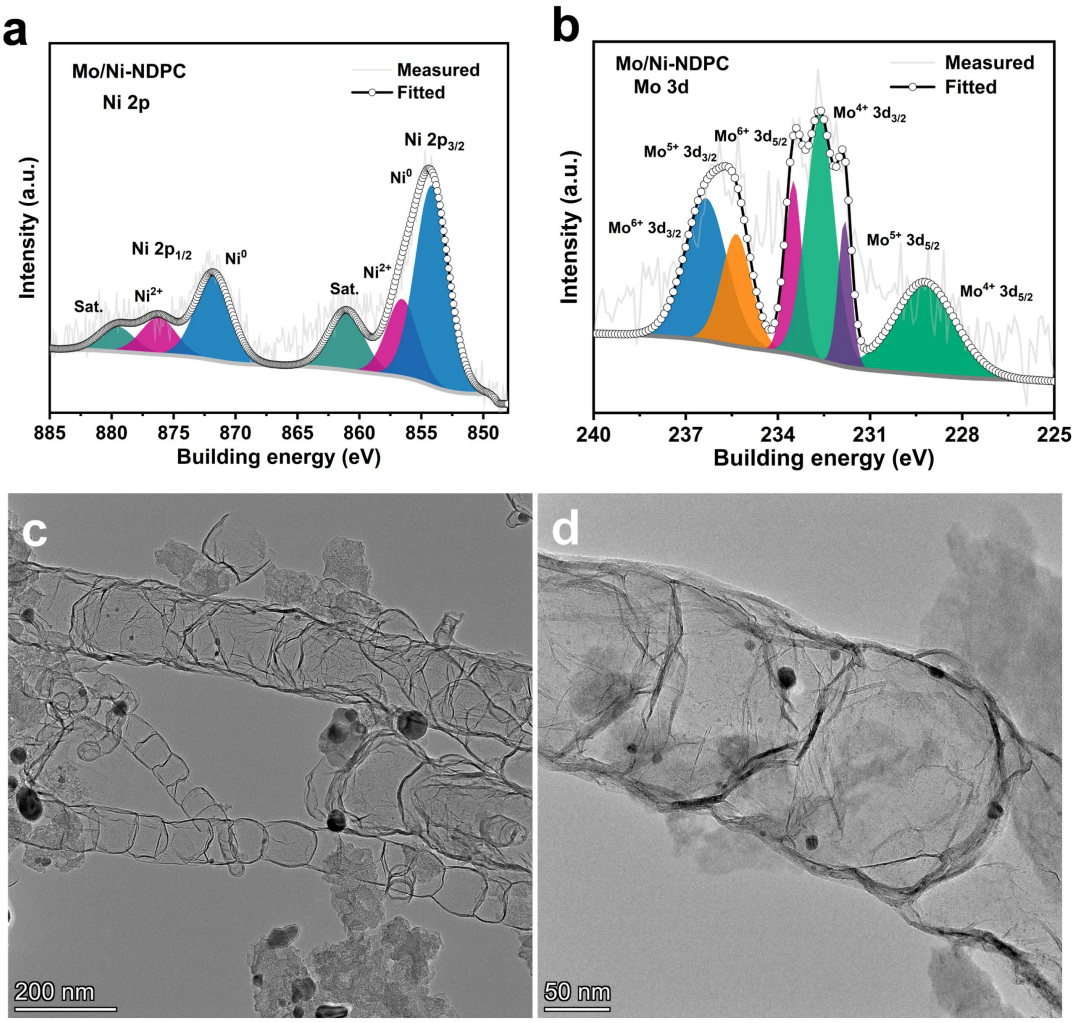


**Figure S10.** XPS spectra of (a) Ni 2p and (b) Mo 3d of Mo/Ni-NDPC after CP measurement; (c-d) TEM of Mo/Ni-NDPC after CP measurement.

**Table S1.** Compilation of BET surface area based on metal modified nitrogen doped carbon-based electrocatalysts under different applications.

| Electrocatalysts | Carbon source | BET surface ($m^2$ $g^{-1}$) | catalytic field | Ref. |
|---|---|---|---|---|
| Co-N-C | ZIF-67 | 395.3 | HRR OER | 1 |
| $Co_{0.75}Fe_{0.25}$-NC | | 334.9 | | |
| $Co_{0.75}Cu_{0.25}$-NC | | 360.5 | | |
| $Co_{0.75}Ni_{0.25}$-NC | | 331.9 | | |
| FeCo@NC | Prussian Blue | 42 | Zn-air battery | 2 |
| Ni@NCx | MOF | 383 | OER | 3 |
| Fe@NCx | | 236 | | |
| NiFe@NCx-P | | 328 | | |
| NiFe@NCx | | 350 | | |
| FeCo@NC | nitrogen doped graphene | 89.2 | HER | 4 |
| Ni@NC | pyromellitic dianhydride | 176.24 | OER | 5 |
| NiFe@NC | | 154.25 | | |
| Fe@NC | Single layer graphene | 188.3 | OER | 6 |
| Co@NC | | 133.5 | | |
| Ni@NC | | 111.6 | | |
| FeCo@NC | | 157.1 | | |
| FeNi@NC | | 168.2 | | |
| CoNi@NC | | 112.1 | | |
| FeCo@NC | ZIF/MIL | 403 | ORR | 7 |
| FeCo/NC | Bulk $C_3N_4$ | 491.9 | ORR/OER | 8 |
| FeCo@NC | 2,2-bipyridine | 263.5 | OER/ORR | 9 |
| Fe-N/C | Dopamine | 384.5 | ORR | 10 |
| Co-N/C | | 417.7 | | |
| FeCo-N/C | | 442.6 | | |
| Ni-NDPC | ZIF-8 | 743.64 | IRR HER | This work |
| Mo/Ni-NDPC | | 636.42 | | |
| Cu/Ni-NDPC | | 494.32 | | |
| Fe/Ni-NDPC | | 614.42 | | |

**Table. S2** EXAFS data fitting results of the Fe/Ni-NDPC.

| Sample | Absorption edge | Path | R (Å) | CN | $\sigma^2$ (eV) | $\Delta E_0$ | R |
|---|---|---|---|---|---|---|---|
| Fe/Ni-NDPC | Fe K-edge | Fe-N | 2.03 | 2.9 | 0.009 | 3.07 | 0.002 |
| | | Fe-Ni | 2.75 | 0.9 | 0.007 | -1.00 | |
| | Ni K-edge | Ni-N | 1.92 | 2.9 | 0.002 | 4.53 | 0.003 |
| | | Ni-Fe | 2.67 | 0.8 | 0.003 | -0.12 | |

CN is coordination number. R is distance between absorber and backscatter atoms. $\Delta E_0$ (eV), inner potential correction accounts for the difference in the inner potential between the sample and the reference compound. $\sigma^2$ is Debye-Waller factor value to account for both thermal and structural disorders. R factor indicates the goodness of the fit.

**Table S3.** the average and variance of photovoltaic parameters in five solar cells based on Fe/Ni-NDPC, Mo/Ni-NDPC, Cu/Ni-NDPC, Ni-NDPC, and Pt counter electrode catalysts.

| CE | $V_{oc}$ (V) | $J_{sc}$ (mA cm$^{-2}$) | FF (%) | PCE (%) |
|---|---|---|---|---|
| Ni-NDPC | 0.81±0.06 | 13.86±0.97 | 64.10±4.04 | 7.18±0.06 |
| Fe/Ni-NDPC | 0.78±0.01 | 16.08±0.05 | 65.08±0.33 | 8.16±0.05 |
| Cu/Ni-NDPC | 0.75±0.01 | 15.42±0.74 | 65.52±2.57 | 7.61±0.09 |
| Mo/Ni-NDPC | 0.75±0.01 | 15.42±0.11 | 67.86±0.10 | 7.79±0.10 |
| Pt | 0.78±0.01 | 15.04±0.21 | 61.77±0.53 | 7.25±0.06 |

$V_{oc}$: open-circuit voltage, $J_{sc}$: short-circuit current density, FF: fill factor, PCE: power conversion efficiency.

**Table S4**. Comparison of the $\eta_{10}$ and corresponding Tafel slope for the HER of the as-prepared catalysts and reported M-N-C catalysts in alkaline condition.

| Electrocatalysts | Electrode substrate | Carbon source | Overpotential/mV (at 10 mA cm$^{-2}$) | Tafel solpe (mV dec$^{-1}$) | Ref. |
|---|---|---|---|---|---|
| Co-N-C | glassy carbon | polymer | 180 | 59.07 | 11 |
| Co-N-C | carbon paper | polyaniline derived carbon nanofibers | 178 | 102 | 12 |
| Co-N-C | glassy carbon | graphene | 337 | 70 | 13 |
| Co@N-C | glassy carbon | prussian blue | 200 | 112 | 14 |
| Co-N-C | glassy carbon | ZIF-67 | 232 | 133 | 15 |
| Co-N-C/CNT | glassy carbon | ZIF-67, CNTs | 203 | 125 | 16 |
| Co-N-C | glassy carbon | Co-MOF | 255 | 101 | 17 |
| Fe-N-C | | Fe-MOF | 370 | 119 | |
| Ni-N-C | exfoliated graphene foil | dicyandiamide | 307 | 183 | 18 |
| Ni@N-C | cellulose filter paper | phenanthroline | 190 | … | 19 |
| Ni@NC | nickel foam | Ni-MOF | 205 | 160 | 20 |
| $Co_{0.75}Fe_{0.25}$-NC | | ZIF-67 | 202 | 67.96 | 1 |
| CoNi@NC | glassy carbon | graphene spheres | 142 | 104 | 21 |
| FeCoNi@FeNC | glassy carbon | EDTA | 105 | 67 | 22 |
| CoNi@NC | | | 179 | 105 | |
| MoNiNC | nickel foam | resin-F127 | 110 | … | 23 |
| Ni-NDPC | nickel foam | ZIF-8 | 173.8 | 102.0 | In this work |
| Mo/Ni-NDPC | nickel foam | | 117.8 | 81.7 | |
| Cu/Ni-NDPC | nickel foam | | 153.8 | 88.1 | |
| Fe/Ni-NDPC | nickel foam | | 134.8 | 80.9 | |

## Reference


1. Feng, X.; Bo, X.; Guo, L., CoM(M=Fe,Cu,Ni)-embedded nitrogen-enriched porous carbon framework for efficient oxygen and hydrogen evolution reactions. *J. Power Sources* **2018,** *389*, 249-259.

2. Cai, P.; Ci, S.; Zhang, E.; Shao, P.; Cao, C.; Wen, Z., FeCo alloy nanoparticles confined in carbon layers as high-activity and robust cathode catalyst for Zn-Air battery. *Electrochim. Acta* **2016,** *220*, 354-362.

3. Zhu, J.; Xiao, M.; Zhang, Y.; Jin, Z.; Peng, Z.; Liu, C.; Chen, S.; Ge, J.; Xing, W., Metal–organic framework-induced synthesis of ultrasmall encased NiFe nanoparticles coupling with graphene as an efficient oxygen electrode for a rechargeable Zn–Air battery. *ACS Catal.* **2016,** *6* (10), 6335-6342.

4. Yang, Y.; Lun, Z.; Xia, G.; Zheng, F.; He, M.; Chen, Q., Non-precious alloy encapsulated in nitrogen-doped graphene layers derived from MOFs as an active and durable hydrogen evolution reaction catalyst. *Energy Environ. Sci.* **2015,** *8* (12), 3563-3571.

5. Zhang, Z.; Qin, Y.; Dou, M.; Ji, J.; Wang, F., One-step conversion from Ni/Fe polyphthalocyanine to N-doped carbon supported Ni-Fe nanoparticles for highly efficient water splitting. *Nano Energy* **2016,** *30*, 426-433.

6. Cui, X.; Ren, P.; Deng, D.; Deng, J.; Bao, X., Single layer graphene encapsulating non-precious metals as high-performance electrocatalysts for water oxidation. *Energy Environ. Sci.* **2016,** *9* (1), 123-129.

7. He, J.; Gao, T.; Jiang, T.; Mu, B.; Suo, Y.; Zhang, Z.; Su, J., Nonprecious nanoalloys embedded in N-enriched mesoporous carbons derived from a dual-MOF as highly active catalyst towards oxygen reduction reaction. *ChemistrySelect* **2018,** *3* (27), 7913-7920.

8. Wu, N.; Lei, Y.; Wang, Q.; Wang, B.; Han, C.; Wang, Y., Facile synthesis of FeCo@NC core–shell nanospheres supported on graphene as an efficient bifunctional oxygen electrocatalyst. *Nano Res.* **2017,** *10* (7), 2332-2343.

9. Li, C.; Wu, M.; Liu, R., High-performance bifunctional oxygen electrocatalysts for zinc-air batteries over mesoporous Fe/Co-N-C nanofibers with embedding FeCo alloy nanoparticles. *Appl. Catal. B* **2019,** *244*, 150-158.

10. Gao, X.-W.; Yang, J.; Song, K.; Luo, W.-B.; Dou, S.-X.; Kang, Y.-M., Robust FeCo nanoparticles embedded in a N-doped porous carbon framework for high oxygen conversion catalytic activity in alkaline and acidic media. *J. Mater. Chem. A* **2018,** *6* (46), 23445-23456.

11. Lyu, D.; Du, Y.; Huang, S.; Mollamahale, B. Y.; Zhang, X.; Hasan, S. W.; Yu, F.; Wang, S.; Tian, Z. Q.; Shen, P. K., Highly efficient multifunctional Co–N–C electrocatalysts with synergistic effects of Co–N mieties and Co metallic nanoparticles encapsulated in a N-doped carbon matrix for water-splitting and oxygen redox reactions. *ACS Appl. Mater. Interfaces* **2019,** *11* (43), 39809-39819.

12. Wang, Z.-L.; Hao, X.-F.; Jiang, Z.; Sun, X.-P.; Xu, D.; Wang, J.; Zhong, H.-X.; Meng, F.-L.; Zhang, X.-B., C and N hybrid coordination derived Co–C–N complex as a highly efficient electrocatalyst for hydrogen evolution reaction. *J. Am. Chem. Soc.* **2015,** *137* (48), 15070-15073.

13. Fei, H.; Yang, Y.; Peng, Z.; Ruan, G.; Zhong, Q.; Li, L.; Samuel, E. L. G.; Tour, J. M., Cobalt nanoparticles embedded in nitrogen-doped carbon for the hydrogen evolution reaction. *ACS Appl. Mater. Interfaces* **2015,** *7* (15), 8083-8087.

14. Zeng, M.; Liu, Y.; Zhao, F.; Nie, K.; Han, N.; Wang, X.; Huang, W.; Song, X.; Zhong, J.; Li, Y.,

Metallic cobalt nanoparticles encapsulated in nitrogen-enriched graphene shells: Its bifunctional electrocatalysis and application in zinc–air batteries. *Adv. Funct. Mater.* **2016,** *26* (24), 4397-4404.

15. Peng, W.; Zheng, G.; Wang, Y.; Cao, S.; Ji, Z.; Huan, Y.; Zou, M.; Yan, X., Zn doped ZIF67-derived porous carbon framework as efficient bifunctional electrocatalyst for water splitting. *Int. J. Hydrog. Energy* **2019,** *44* (36), 19782-19791.

16. Yang, F.; Zhao, P.; Hua, X.; Luo, W.; Cheng, G.; Xing, W.; Chen, S., A cobalt-based hybrid electrocatalyst derived from a carbon nanotube inserted metal–organic framework for efficient water-splitting. *J. Mater. Chem. A* **2016,** *4* (41), 16057-16063.

17. Wang, Y.; Pan, Y.; Zhu, L.; Yu, H.; Duan, B.; Wang, R.; Zhang, Z.; Qiu, S., Solvent-free assembly of Co/Fe-containing MOFs derived N-doped mesoporous carbon nanosheets for ORR and HER. *Carbon* **2019,** *146*, 671-679.

18. Lei, C.; Wang, Y.; Hou, Y.; Liu, P.; Yang, J.; Zhang, T.; Zhuang, X.; Chen, M.; Yang, B.; Lei, L.; Yuan, C.; Qiu, M.; Feng, X., Efficient alkaline hydrogen evolution on atomically dispersed Ni–$N_x$ Species anchored porous carbon with embedded Ni nanoparticles by accelerating water dissociation kinetics. *Energy Environ. Sci.* **2019,** *12* (1), 149-156.

19. Ren, J.; Antonietti, M.; Fellinger, T.-P., Efficient water splitting using a simple Ni/N/C paper electrocatalyst. *Adv. Energy Mater.* **2015,** *5* (6), 1401660.

20. Xu, Y.; Tu, W.; Zhang, B.; Yin, S.; Huang, Y.; Kraft, M.; Xu, R., Nickel nanoparticles encapsulated in few-layer nitrogen-doped graphene derived from metal–organic frameworks as efficient bifunctional electrocatalysts for overall water splitting. *Adv. Mater.* **2017,** *29* (11), 1605957.

21. Deng, J.; Ren, P.; Deng, D.; Bao, X., Enhanced electron penetration through an ultrathin graphene layer for highly efficient catalysis of the hydrogen evolution reaction. *Angew. Chem. Int. Ed.* **2015,** *54* (7), 2100-2104.

22. Zhang, Q.; Webster, R. F.; Cheong, S.; Tilley, R. D.; Lu, X.; Amal, R., Ultrathin Fe-N-C nanosheets coordinated Fe-doped CoNi alloy nanoparticles for electrochemical water splitting. *Particle & Particle Systems Characterization* **2019,** *36* (1), 1800252.

23. Wang, F.; Sun, Y.; He, Y.; Liu, L.; Xu, J.; Zhao, X.; Yin, G.; Zhang, L.; Li, S.; Mao, Q.; Huang, Y.; Zhang, T.; Liu, B., Highly efficient and durable MoNiNC catalyst for hydrogen evolution reaction. *Nano Energy* **2017,** *37*, 1-6.